

Research Article

Stefan Burger, Thomas Franke, Thomas Fraunholz, Ronald H. W. Hoppe,
Malte A. Peter and Achim Wixforth

Numerical Simulation of Surface Acoustic Wave Actuated Separation of Rigid Enantiomers by the Fictitious Domain Lagrange Multiplier Method

Abstract: Enantiomers are chiral objects which differ by their orientation and are thus referred to as left-handed and right-handed enantiomers. In applications they mostly occur as so-called racemic compounds consisting of approximately the same amount of left- and right-handed species which may have completely different properties. Hence, the separation of left- from right-handed enantiomers is an important issue. Conventional technologies are based on gas or high pressure liquid chromatography, capillary electrophoresis, or nuclear magnetic resonance, but typically they are slow and require costly chiral media. A new idea for separation of chiral objects is based on introducing them in certain vorticity patterns, which has been shown to work in theory for an extremely simplified setting by Kostur et al. [14]. In this paper, we investigate whether these ideas can be successfully adapted to a more realistic setup which can be implemented experimentally. For this purpose, we simulate transport of rigid chiral particles in a fluidic environment by an application of the fictitious domain Lagrange multiplier method due to Glowinski et al. [11] which has been designed to study the motion of rigid particles in carrier fluids. Numerical results are presented which illustrate the feasibility of enantiomer separation in flow fields consisting of pairwise counter-rotating vortices. Moreover, a first experimental setup based on surface acoustic wave generated vorticity patterns on the surface of a carrier fluid is devised which reflects the idealized numerical model and gives promising results with respect to properties of particle propagation. These findings may lead to a new technology for enantiomer separation which is both fast and cost-effective.

Keywords: Enantiomer Separation, Surface Acoustic Waves, Fictitious Domain Lagrange Multiplier Method

MSC 2010: 65M60, 74L15, 76Z05, 92C10, 92C50

DOI: 10.1515/cmam-2015-0009

Received February 2, 2015; revised March 1, 2015; accepted March 4, 2015

1 Introduction

Enantiomers are chiral geometric objects where an object is said to be chiral, if it is not identical to its mirror image. Since the word chiral stems from the Greek ‘ $\chi\epsilon\rho$ ’ which means ‘hand’, one distinguishes enantiomers

Stefan Burger, Thomas Franke, Achim Wixforth: Institute of Physics, University of Augsburg, 86159 Augsburg, Germany, e-mail: stefan.burger@physik.uni-augsburg.de, thomas.franke@physik.uni-augsburg.de, achim.wixforth@physik.uni-augsburg.de

Thomas Fraunholz: Institute of Mathematics, University of Augsburg, 86159 Augsburg, Germany, e-mail: thomas.fraunholz@math.uni-augsburg.de

Ronald H. W. Hoppe: Institute of Mathematics, University of Augsburg, 86159 Augsburg, Germany; and Department of Mathematics, University of Houston, Houston, TX 77204-3008, USA, e-mail: rohop@math.uh.edu

Malte A. Peter: Institute of Mathematics and Augsburg Centre for Innovative Technologies, University of Augsburg, 86159 Augsburg, Germany, e-mail: peter@math.uni-augsburg.de

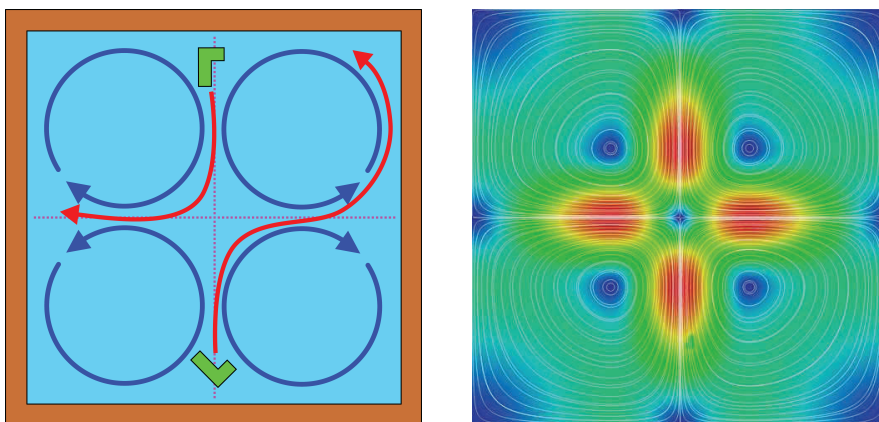


Figure 1. Sketch of the anticipated separation process of L-shaped enantiomers by pairwise counter-rotating vortices (left) and employed vorticity pattern (right).

by their handedness (right- resp. left-handedness). In chemistry, chirality refers to a molecule which is not superposable on its mirror image. Compounds consisting of molecules of the same handedness are called enantiopure or unichiral, whereas compounds consisting of the same amount of right- and left-handed enantiomers are referred to as racemic. The discovery of inorganic molecular chirality goes back to the physicists Biot and Gay-Lussac as well as the chemist and microbiologist Pasteur, whereas organic molecular chirality has been discovered by van't Hoff and LeBel. First models for chiral molecules based on electronic theories have been developed by Born, Condon, and Hund, whereas more recent models rely on parity violation in electro-weak quantum chemistry (cf. [20] and the references therein). Since the chemical synthesis of enantiomers usually gives rise to racemic compounds, enantiomer separation plays a significant role in agrochemical, electronic, and pharmaceutical as well as food, flavor and fragrance industries (cf., e.g., [3, 7–9, 15]). Traditional separation technologies are based on gas or high pressure liquid chromatography [5, 25], capillary electrophoresis [21], or nuclear magnetic resonance [26], but most of them are slow and require costly chiral media.

A different approach uses the fact that enantiomers drift in microflows with a direction depending on their chirality [5, 16, 18]. In particular, enantiomer separation using a quadrupolar force field was previously predicted in [14] from a theoretical point of view for simple idealized chiral objects.

This paper is devoted to applying these ideas to a setup which can be developed experimentally and to testing this setup both numerically and experimentally. The idea is to use a quadrupolar force field to create a two-dimensional fluid flow (at the surface of a bulk fluid) in which floating shallow enantiomers are separated using pairwise counter-rotating vortices. The general separation mechanism is sketched in Figure 1 (left) while the used flow field (without enantiomers) is shown in Figure 1 (right).

The numerical simulation of this separation process at the (two-dimensional) fluid surface is performed by an adaption of the fictitious domain Lagrange multiplier method (FDLM) which has been developed by Glowinski et al. [11] and successfully applied to the sedimentation of rigid bodies in fluid containers [19] and the numerical simulation of the rheology of red blood cells in microvessels [24]. Using this method, we perform fluid–structure interaction simulations using L-shaped objects, rigid enantiomers, in a fluid environment. In particular, we identify the separation mechanism.

In the experiment, the counter-rotating vortices are actuated by surface acoustic waves (SAWs). More precisely, the setup consists of a fluid-filled container put on top of a plate partially coated with a piezoelectric material and an Inter-Digital Transducer (IDT) appropriately placed in the middle of the bottom of the container. Applying a high-frequency signal to the IDT, due to the piezoelectric effect surface acoustic waves (SAWs) are generated that enter the container and create a vorticity pattern consisting of pairwise counter-rotating vortices. As test enantiomers, we use photoresist made, L-shaped, rigid particles floating on the surface of the fluid. The experimental results validate the numerical model in terms of transport characteristics.

The paper is organized as follows: In Section 2, we present the adaption of the FDLM to the separation of the enantiomers on the surface of the fluid, whereas Section 3 is devoted to the numerical realization of the FDLM. Section 4 contains a description of the experimental setup and a comparison of the numerical simulations with experimental data. In Section 5, we provide a documentation of numerical simulations for the enantiomer separation revealing the separation mechanism. Conclusions are given in Section 6.

2 The Numerical Model Based on the Fictitious Domain Lagrange Multiplier Method (FDLM)

Based on the work of Kostur et al. [14], we want to investigate whether separation of rigid chiral particles can be achieved by introducing them into a two-dimensional flow field which is driven by a quadrupolar force field. In view of the experimental setup devised in Section 4, we think of this two-dimensional domain as the surface of a fluid volume, at which the particles float.

For the numerical simulation of the enantiomer separation on the surface Γ_s of the fluid, the advantage of the fictitious domain Lagrange multiplier approach is that the computations can be performed on a fixed mesh of the spatial domain Γ_s by imposing distributed Lagrange multipliers to the fluid on the domains occupied by the enantiomers.

We assume that N moving rigid, L-shaped enantiomers have been injected onto the surface Γ_s of the fluid occupying subdomains $B_j(t) \subset \Gamma_s$, $1 \leq j \leq N$, with $B_j(t) \cap B_k(t) = \emptyset$, $1 \leq j \neq k \leq N$, $t \in (0, T)$. We refer to ρ_j , M_j , \mathbf{C}_j , Θ_j , \mathbf{v}_j , and $\boldsymbol{\omega}_j$, $j \in \{1, \dots, N\}$, as the density, mass, center of mass, angle, velocity of the center of mass, and the angular velocity of the j -th enantiomer. Moreover, \mathbf{I}_j , \mathbf{F}_j^H , \mathbf{F}_j^r , \mathbf{T}_j^H stand for the inertia tensor, the resultant of the hydrodynamic forces, the artificial repulsive forces, and the torque at \mathbf{C}_j of the hydrodynamic forces acting on the j -th enantiomer. In particular, the repulsive forces \mathbf{F}_j^r , $1 \leq j \leq N$, are given by

$$\mathbf{F}_j^r = \sum_{k \neq j} \mathbf{F}_{jk}^P + \mathbf{F}_j^{\partial\Gamma_s},$$

where \mathbf{F}_{jk}^P is the repulsive force between the j -th enantiomer and the other enantiomers and $\mathbf{F}_j^{\partial\Gamma_s}$ is the repulsive force between the j -th enantiomer and the wall of the fluid container according to

$$\mathbf{F}_j^{\partial\Gamma_s} := \sum_{\mathbf{p}_i \in \mathbf{P}_j} \sum_{\mathbf{p}_l \in \mathbf{P}^{\partial\Gamma_s}} \mathbf{F}^r(\mathbf{p}_i, \mathbf{p}_l), \quad (1a)$$

$$\mathbf{F}_{jk}^P := \sum_{\mathbf{p}_i \in \mathbf{P}_j} \sum_{\mathbf{p}_l \in \mathbf{P}_k} \mathbf{F}^r(\mathbf{p}_i, \mathbf{p}_l), \quad (1b)$$

$$\mathbf{F}^r(\mathbf{p}_i, \mathbf{p}_l) := \begin{cases} 0 & \text{if } d_{il} > r, \\ \varepsilon^{-1}(\mathbf{p}_i - \mathbf{p}_l)/d_{il}(r - d_{il})^2 & \text{if } d_{il} < r. \end{cases} \quad (1c)$$

Here, $r > 0$ is some distance, called the repulsion length, usually chosen discretization dependent as one half of the mesh width of the finite element mesh for the discretization of the Navier–Stokes equations. Moreover, \mathbf{P}_j and $\mathbf{P}^{\partial\Gamma_s}$ denote the sets of vertices belonging to the j -th particle and $\partial\Gamma_s$, respectively. In addition to this, ε is used as a scaling factor and $d_{il} := \text{dist}(\mathbf{p}_i, \mathbf{p}_l)$ denotes the distance between two points. Setting $\Gamma_s(t) := \Gamma_s \setminus \bigcup_{j=1}^N \overline{B_j(t)}$, the velocity \mathbf{v} and pressure p of the fluid is modeled by the incompressible Navier–Stokes equations

$$\rho_f \frac{\partial \mathbf{v}}{\partial t} + \rho_f (\mathbf{v} \cdot \nabla) \mathbf{v} - \eta \nabla^2 \mathbf{v} - \nabla p = \mathbf{f}, \quad x \in \Gamma_s(t), \quad t \in (0, T), \quad (2a)$$

$$\nabla \cdot \mathbf{v} = 0, \quad x \in \Gamma_s(t), \quad t \in (0, T), \quad (2b)$$

with fluid density ρ_f , dynamic viscosity η , boundary conditions

$$\mathbf{v}(x, t) = \begin{cases} \hat{\mathbf{v}} & \text{if } x \in \partial\Gamma_s, \quad t \in (0, T), \\ \mathbf{v}_j(t) + \boldsymbol{\omega}_j(t) \times \overrightarrow{\mathbf{C}_j(t)x} & \text{if } x \in \partial B_j(t), \quad t \in (0, T), \end{cases} \quad (2c)$$

and initial condition

$$\mathbf{v}(x, 0) = \hat{\mathbf{v}}, \quad x \in \Gamma_s(0). \quad (2d)$$

Note that $\overrightarrow{\mathbf{C}_j(t)x}$ in (2c) refers to the vector joining $\mathbf{C}_j(t)$ and x , and \mathbf{f} in (2a) stands for an external force density.

The motion of the N enantiomers is described by the Newton–Euler equations

$$M_j \frac{d\mathbf{v}_j}{dt} = \mathbf{F}_j^H + \mathbf{F}_j^r, \quad \frac{d\mathbf{C}_j}{dt} = \mathbf{v}_j(t), \quad \frac{d\Theta_j}{dt} = \boldsymbol{\omega}_j, \quad 1 \leq j \leq N, \quad (3a)$$

$$\mathbf{I}_j \frac{d\boldsymbol{\omega}_j}{dt} = \mathbf{T}_j^H + \overrightarrow{\mathbf{C}_j x} \times \mathbf{F}_j^r, \quad 1 \leq j \leq N, \quad (3b)$$

with initial conditions

$$\mathbf{v}_j(0) = \mathbf{v}_j^0, \quad \boldsymbol{\omega}_j(0) = \boldsymbol{\omega}_j^0, \quad \mathbf{C}_j(0) = \mathbf{C}_j^0, \quad 1 \leq j \leq N. \quad (3c)$$

Rigid body motions are imposed to the fluid in $B_j(t)$, $1 \leq j \leq N$, which is taken care of by distributed Lagrange multipliers $\boldsymbol{\lambda}_j(t) \in \boldsymbol{\Lambda}_j(t) := \mathbf{H}^1(B_j(t))$, $1 \leq j \leq N$, where here and in the sequel we use standard notation from Lebesgue and Sobolev space theory [22].

The numerical model based on the FDLM method above therefore amounts to the computation of $\mathbf{v}(t) \in \mathbf{V} := \{\mathbf{H}^1(\Gamma_s) \mid \mathbf{v}|_{\partial\Gamma_s} = \hat{\mathbf{v}}\}$, $p(t) \in L_0^2(\Gamma_s)$, $\mathbf{v}_j(t), \mathbf{C}_j(t) \in \mathbb{R}^2$, $\boldsymbol{\omega}_j(t) \in \mathbb{R}$, $\boldsymbol{\lambda}_j(t) \in \boldsymbol{\Lambda}_j(t)$, $1 \leq j \leq N$, such that for all $\mathbf{w} \in \mathbf{H}_0^1(\Gamma_s)$, $q \in L_0^2(\Gamma_s)$, $\mathbf{Y} \in \mathbb{R}^2$, $\boldsymbol{\tau} \in \mathbb{R}$, $\boldsymbol{\mu}_j \in \boldsymbol{\Lambda}_j(t)$, $1 \leq j \leq N$, there holds

$$\begin{aligned} & \rho_f \int_{\Gamma_s} \left(\frac{\partial \mathbf{v}}{\partial t} + (\mathbf{v} \cdot \nabla) \mathbf{v} \right) \cdot \mathbf{w} \, dx - \int_{\Gamma_s} p \nabla \cdot \mathbf{w} \, dx + \eta \int_{\Gamma_s} \nabla \mathbf{v} : \nabla \mathbf{w} \, dx + \sum_{j=1}^N \left(1 - \frac{\rho_f}{\rho_j} \right) \left(M_j \frac{d\mathbf{v}_j}{dt} \cdot \mathbf{Y} + \mathbf{I}_j \frac{d\boldsymbol{\omega}_j}{dt} \cdot \boldsymbol{\tau} \right) \\ & = \sum_{j=1}^N \int_{B_j(t)} \left(\boldsymbol{\lambda}_j \cdot (\mathbf{w} - \mathbf{Y} - \boldsymbol{\tau} \times \overrightarrow{\mathbf{C}_j x}) \right) + \rho_f \int_{\Gamma_s} \mathbf{f} \cdot \mathbf{w} \, dx + \sum_{j=1}^N \left((\mathbf{F}_j^H + \mathbf{F}_j^r) \cdot \mathbf{Y} + (\mathbf{T}_j^H + \mathbf{F}_j^r \times \overrightarrow{\mathbf{C}_j x}) \cdot \boldsymbol{\tau} \right), \end{aligned} \quad (4a)$$

$$\int_{\Gamma_s} q \nabla \cdot \mathbf{v} \, dx = 0, \quad (4b)$$

$$\int_{B_j(t)} \left(\boldsymbol{\mu}_j \cdot (\mathbf{v} - \mathbf{v}_j - \boldsymbol{\omega}_j \times \overrightarrow{\mathbf{C}_j x}) \right) dx = 0, \quad 1 \leq j \leq N, \quad (4c)$$

with initial conditions

$$\mathbf{v}(x, 0) = \begin{cases} \hat{\mathbf{v}} & \text{if } x \in \Gamma_s(0) \setminus \overline{B_j(0)}, \\ \mathbf{v}_j^0 + \boldsymbol{\omega}_j^0 \times \overrightarrow{\mathbf{C}_j x} & \text{if } x \in \overline{B_j(0)}, \end{cases} \quad (4d)$$

$$\mathbf{v}_j(0) = \mathbf{v}_j^0, \quad \mathbf{C}_j(0) = \mathbf{C}_j^0, \quad \boldsymbol{\omega}_j(0) = \boldsymbol{\omega}_j^0, \quad B_j(0) = B_j^0, \quad 1 \leq j \leq N. \quad (4e)$$

3 Discretization and Numerical Solution

In this section, we describe the discretization of (2) and (4) in space and time. For the spatial discretization of the incompressible Navier–Stokes equations (2) we use Taylor–Hood P2/P1 elements [4] with respect to a quasiuniform simplicial triangulation $\mathcal{T}_h(\Gamma_s)$ of the computational domain Γ_s . For $K \in \mathcal{T}_h(\Gamma_s)$, we denote by $|K|$ the area of K , by h_K the diameter of K , and we set $h := \max\{h_K \mid K \in \mathcal{T}_h(\Gamma_s)\}$. Further, $P_k(K)$, $k \in \mathbb{N}$, refers to the set of polynomials of degree $\leq k$ on K . The finite element trial spaces \mathbf{V}_h for the velocity and Q_h for the pressure read

$$\begin{aligned} \mathbf{V}_h & := \{ \mathbf{v}_h \in \mathbf{C}(\bar{\Gamma}_s) \mid \mathbf{v}_h|_K \in P_2(K)^2, \, K \in \mathcal{T}_h(\Gamma_s), \, \mathbf{v}_h|_{\partial\Gamma_s} = \hat{\mathbf{v}}_h \}, \\ Q_h & := \{ w_h \in C(\bar{\Gamma}_s) \mid w_h|_K \in P_1(K), \, K \in \mathcal{T}_h(\Gamma_s), \, \int_{\Gamma_s} w_h \, dx = 0 \}, \end{aligned}$$

where $\hat{\mathbf{v}}_h$ is the L^2 -projection of $\hat{\mathbf{v}}$ onto the space of piecewise polynomials of degree 2 on $\partial\Gamma_s$. We further refer to

$$\mathbf{V}_{h,0} := \{\mathbf{v}_h \in \mathbf{C}(\bar{\Gamma}_s) \mid \mathbf{v}_h|_K \in P_2(K)^2, K \in \mathcal{T}_h(\Gamma_s), \mathbf{v}_h|_{\partial\Gamma_s} = \mathbf{0}\}$$

as the associated finite element test space for the velocity.

We avoid an additional triangulation $\mathcal{T}_h(B_j(t))$, $1 \leq j \leq N$, of the domains occupied by the enantiomers. Instead, we use the domains $B_{h,j}(t) \subset \mathcal{T}_h$ consisting of all $K \in \mathcal{T}_h$ with $K \subset B_j(t)$. The finite element spaces $\Lambda_{h,j}(t)$ for the distributed Lagrange multipliers are chosen according to

$$\Lambda_{h,j}(t) := \{\lambda_h \in \mathbf{C}(B_j(t)) \mid \lambda_h|_K \in P_2(K)^2\}, \quad 1 \leq j \leq N.$$

The algorithm requires the computation of $\mathbf{v}_h(t) \in \mathbf{V}_h$, $p_h(t) \in Q_h$, $\mathbf{v}_j(t)$, $\mathbf{C}_j(t) \in \mathbb{R}^2$, $\boldsymbol{\omega}_j(t) \in \mathbb{R}$, $\lambda_{h,j}(t) \in \Lambda_{h,j}(t)$, $1 \leq j \leq N$, such that for all $\mathbf{w}_h \in \mathbf{V}_{h,0}$, $q_h \in Q_h$, $\mathbf{Y} \in \mathbb{R}^2$, $\boldsymbol{\tau} \in \mathbb{R}$, $\boldsymbol{\mu}_{h,j} \in \Lambda_{h,j}(t)$, $1 \leq j \leq N$, it holds

$$\begin{aligned} & \rho_f \int_{\Gamma_s} \left(\frac{\partial \mathbf{v}_h}{\partial t} + (\mathbf{v}_h \cdot \nabla) \mathbf{v}_h \right) \cdot \mathbf{w}_h \, dx - \int_{\Gamma_s} p_h \nabla \cdot \mathbf{w}_h \, dx + \eta \int_{\Gamma_s} \nabla \mathbf{v}_h : \nabla \mathbf{w}_h \, dx + \sum_{j=1}^N \left(1 - \frac{\rho_f}{\rho_j} \right) \left(M_j \frac{d\mathbf{v}_j}{dt} \cdot \mathbf{Y} + \mathbf{I}_j \frac{d\boldsymbol{\omega}_j}{dt} \cdot \boldsymbol{\tau} \right) \\ & = \sum_{j=1}^N \int_{B_{h,j}(t)} \left(\lambda_{h,j} \cdot (\mathbf{w}_h - \mathbf{Y} - \boldsymbol{\tau} \times \overrightarrow{\mathbf{C}_j x}) \right) dx + \rho_f \int_{\Gamma_s} \mathbf{f} \cdot \mathbf{w}_h \, dx + \sum_{j=1}^N \left((\mathbf{F}_j^H + \mathbf{F}_j^r) \cdot \mathbf{Y} + (\mathbf{T}_j^H + \mathbf{F}_j^r \times \overrightarrow{\mathbf{C}_j x}) \cdot \boldsymbol{\tau} \right), \end{aligned} \quad (5a)$$

$$\int_{\Gamma_s} q_h \nabla \cdot \mathbf{v}_h \, dx = 0, \quad (5b)$$

$$\int_{B_{h,j}(t)} \left(\boldsymbol{\mu}_{h,j} \cdot (\mathbf{v}_h - \mathbf{v}_j - \boldsymbol{\omega}_j \times \overrightarrow{\mathbf{C}_j x}) \right) dx = 0, \quad 1 \leq j \leq N, \quad (5c)$$

with initial conditions

$$\mathbf{v}_h(x, 0) = \begin{cases} \hat{\mathbf{v}}_h & \text{if } x \in \Gamma_s(0) \setminus \overline{B_j(0)}, \\ \mathbf{v}_j^0 + \boldsymbol{\omega}_j^0 \times \overrightarrow{\mathbf{C}_j^0 x} & \text{if } x \in \overline{B_j(0)}, \end{cases} \quad (5d)$$

$$\mathbf{v}_j(0) = \mathbf{v}_j^0, \quad \mathbf{C}_j(0) = \mathbf{C}_j^0, \quad \boldsymbol{\omega}_j(0) = \boldsymbol{\omega}_j^0, \quad B_j(0) = B_j^0, \quad 1 \leq j \leq N, \quad (5e)$$

where $\hat{\mathbf{v}}_h$ is the L^2 -projection of $\hat{\mathbf{v}}$ onto \mathbf{V}_h .

For the discretization in time we use the Yanenko–Marchuk fractional step method [17] which gives rise to the solution of elliptic subproblems that are taken care of by the conjugate gradient method. We assume a partition $\{0 := t_0 < t_1 < \dots < t_N := T\}$ of the time interval $[0, T]$ into subintervals $[t_{n-1}, t_n]$ of length $\Delta t_n := t_n - t_{n-1}$ and denote by \mathbf{x}^n an approximation of the variable \mathbf{x} at time t_n . In order to propagate from time t_{n-1} to t_n , we proceed in three major steps similar to [11]. First, we solve the fluid motion part of (5a) by using the splitting method proposed by Chorin and Temam [6, 23]. This means we compute a tentative velocity $\tilde{\mathbf{v}}_h \in \mathbf{V}_h$ such that for all $\mathbf{w}_h \in \mathbf{V}_{h,0}$ there holds

$$\rho_f \int_{\Gamma_s} \left((\tilde{\mathbf{v}}_h - \mathbf{v}_h^{n-1}) / \Delta t_n \right) \cdot \mathbf{w}_h \, dx + \rho_f \int_{\Gamma_s} (\nabla \mathbf{v}_h^{n-1} \cdot \mathbf{v}_h^{n-1}, \mathbf{w}_h) \, dx + \eta \int_{\Gamma_s} \nabla \mathbf{v}_h^{n-1} \cdot \nabla \mathbf{w}_h \, dx = \rho_f \int_{\Gamma_s} \mathbf{f} \cdot \mathbf{w}_h \, dx.$$

For proper iterative solutions $\mathbf{v}_h^{n-1/2} \in \mathbf{V}_h$ and $p_h^n \in Q_h$ we have to project the tentative velocity $\tilde{\mathbf{v}}_h$ onto the space of divergence free vector fields. Therefore, we solve the following equations:

$$\begin{aligned} \Delta t_n \int_{\Gamma_s} \nabla p_h^n \cdot \nabla q_h \, dx &= - \int_{\Gamma_s} (\nabla \cdot \tilde{\mathbf{v}}_h) q_h, \\ \int_{\Gamma_s} \mathbf{v}_h^{n-1/2} \cdot \mathbf{w}_h \, dx &= \int_{\Gamma_s} \tilde{\mathbf{v}}_h \cdot \mathbf{w}_h \, dx - \Delta t_n \int_{\Gamma_s} \nabla p_h^n \cdot \mathbf{w}_h \, dx, \end{aligned}$$

which have to be satisfied for all $\mathbf{w}_h \in \mathbf{V}_{h,0}$ and $q_h \in Q_h$. In the next step, we take care of the fluid-particle interaction which can be written as a subproblem of (5) such that for all $\mathbf{w}_h \in \mathbf{V}_{h,0}$, $\mathbf{Y} \in \mathbb{R}^2$, $\boldsymbol{\tau} \in \mathbb{R}$, $\boldsymbol{\mu}_{h,j} \in \Lambda_{h,j}(t)$,

$1 \leq j \leq N$, it holds

$$\rho_f \int_{\Gamma_s} \frac{\partial \mathbf{v}_h}{\partial t} dx + \sum_{j=1}^N \left(1 - \frac{\rho_f}{\rho_j}\right) \left(M_j \frac{d\mathbf{v}_j}{dt} \cdot \mathbf{Y} + \mathbf{I}_j \frac{d\boldsymbol{\omega}_j}{dt} \cdot \boldsymbol{\tau}\right) = \sum_{j=1}^N \int_{B_{h,j}(t)} \left(\boldsymbol{\lambda}_{h,j} \cdot (\mathbf{w}_h - \mathbf{Y} - \boldsymbol{\tau} \times \overrightarrow{\mathbf{C}_j \chi})\right) dx,$$

$$\int_{B_{h,j}(t)} \left(\boldsymbol{\mu}_{h,j} \cdot (\mathbf{v}_h - \mathbf{v}_j - \boldsymbol{\omega}_j \times \overrightarrow{\mathbf{C}_j \chi})\right) dx = 0, \quad 1 \leq j \leq N,$$

Following [11] we use the conjugate gradient algorithm for solving this problem. The initialization step $s = 0$ is:

$$\rho_f \int_{\Gamma_s} \frac{\mathbf{v}_h^{\text{init}} - \mathbf{v}_h^{n-1/2}}{\Delta t} \cdot \mathbf{w}_h dx = \sum_{j=1}^N \int_{B_{h,j}^{n-1}} \boldsymbol{\lambda}_{h,j}^{n-1} \cdot \mathbf{w}_h dx, \quad (6a)$$

$$\left(1 - \frac{\rho_f}{\rho_j}\right) M_j \frac{\mathbf{v}_j^{\text{init}} - \mathbf{v}_j^{n-1}}{\Delta t} \cdot \mathbf{Y} = - \int_{B_{h,j}^{n-1}} \boldsymbol{\lambda}_{h,j}^{n-1} \cdot \mathbf{Y} dx, \quad 1 \leq j \leq N, \quad (6b)$$

$$\left(1 - \frac{\rho_f}{\rho_j}\right) \mathbf{I}_j \frac{\boldsymbol{\omega}_j^{\text{init}} - \boldsymbol{\omega}_j^{n-1}}{\Delta t} \cdot \boldsymbol{\tau} = - \int_{B_{h,j}^{n-1}} \boldsymbol{\lambda}_{h,j}^{n-1} \cdot \boldsymbol{\tau} \times \overrightarrow{\mathbf{C}_j \chi} dx, \quad 1 \leq j \leq N. \quad (6c)$$

Then, for $1 \leq j \leq N$ we compute

$$\int_{B_{h,j}^{n-1}} \boldsymbol{\mu}_{h,j} \cdot \mathbf{g}_{h,j}^{\text{init}} dx = \int_{B_{h,j}^{n-1}} \left(\boldsymbol{\mu}_{h,j} \cdot (\mathbf{v}_h^{\text{init}} - \mathbf{v}_j^{\text{init}} - \boldsymbol{\omega}_j^{\text{init}} \times \overrightarrow{\mathbf{C}_j \chi})\right) dx = 0, \quad (6d)$$

and set $\mathbf{z}_{h,j}^{\text{init}} = \mathbf{g}_{h,j}^{\text{init}}$. For the following steps $s > 0$, we assume $\boldsymbol{\lambda}_{h,j}^{s-1}$, \mathbf{v}_h^{s-1} , \mathbf{v}_j^{s-1} , $\boldsymbol{\omega}_j^{s-1}$, $\mathbf{z}_{h,j}^{s-1}$ and $\mathbf{g}_{h,j}^{s-1}$ to be known. In order to obtain $\boldsymbol{\lambda}_{h,j}^s$, \mathbf{v}_h^s , \mathbf{v}_j^s , $\boldsymbol{\omega}_j^s$, $\mathbf{z}_{h,j}^s$ and $\mathbf{g}_{h,j}^s$ by a descent step, we need to solve

$$\rho_f \int_{\Gamma_s} \frac{\mathbf{v}_h^{\text{desc}}}{\Delta t} \cdot \mathbf{w}_h dx = \sum_{j=1}^N \int_{B_{h,j}^{n-1}} \mathbf{z}_{h,j}^{s-1} \cdot \mathbf{w}_h dx, \quad (7a)$$

$$\left(1 - \frac{\rho_f}{\rho_j}\right) M_j \frac{\mathbf{v}_j^{\text{desc}}}{\Delta t} \cdot \mathbf{Y} = - \int_{B_{h,j}^{n-1}} \mathbf{z}_{h,j}^{s-1} \cdot \mathbf{Y} dx, \quad 1 \leq j \leq N, \quad (7b)$$

$$\left(1 - \frac{\rho_f}{\rho_j}\right) \mathbf{I}_j \frac{\boldsymbol{\omega}_j^{\text{desc}}}{\Delta t} \cdot \boldsymbol{\tau} = - \int_{B_{h,j}^{n-1}} \mathbf{z}_{h,j}^{s-1} \cdot \boldsymbol{\tau} \times \overrightarrow{\mathbf{C}_j \chi} dx, \quad 1 \leq j \leq N, \quad (7c)$$

and then

$$\int_{B_{h,j}^{n-1}} \boldsymbol{\mu}_{h,j} \cdot \mathbf{g}_{h,j}^{\text{desc}} dx = \int_{B_{h,j}^{n-1}} \left(\boldsymbol{\mu}_{h,j} \cdot (\mathbf{v}_h^{\text{desc}} - \mathbf{v}_j^{\text{desc}} - \boldsymbol{\omega}_j^{\text{desc}} \times \overrightarrow{\mathbf{C}_j \chi})\right) dx = 0, \quad 1 \leq j \leq N, \quad (7d)$$

Finally, we update our variables by computing

$$\rho_j^{s-1} = \frac{\int_{B_{h,j}^{n-1}} \mathbf{g}_{h,j}^{s-1} \cdot \mathbf{g}_{h,j}^{s-1} dx}{\int_{B_{h,j}^{n-1}} (\mathbf{z}_{h,j}^{s-1} \cdot (\mathbf{v}_h^{\text{desc}} - \mathbf{v}_j^{\text{desc}} - \boldsymbol{\omega}_j^{\text{desc}} \times \overrightarrow{\mathbf{C}_j \chi})) dx}, \quad 1 \leq j \leq N, \quad (7e)$$

and setting

$$\begin{aligned} \boldsymbol{\lambda}_{h,j}^s &= \boldsymbol{\lambda}_{h,j}^{s-1} - \rho_j^{s-1} \mathbf{z}_{h,j}^{s-1}, \\ \mathbf{v}_h^s &= \mathbf{v}_h^{s-1} - \rho_j^{s-1} \mathbf{v}_h^{\text{desc}}, \\ \mathbf{v}_j^s &= \mathbf{v}_j^{s-1} - \rho_j^{s-1} \mathbf{v}_j^{\text{desc}}, \\ \boldsymbol{\omega}_j^s &= \boldsymbol{\omega}_j^{s-1} - \rho_j^{s-1} \boldsymbol{\omega}_j^{\text{desc}}, \\ \mathbf{g}_{h,j}^s &= \mathbf{g}_{h,j}^{s-1} - \rho_j^{s-1} \mathbf{g}_{h,j}^{\text{desc}}. \end{aligned}$$

The last step of the conjugate gradient algorithm is to test convergence and to construct a new descent direction. To this end, if

$$\frac{\int_{B_{h,j}^{n-1}} \mathbf{g}_{h,j}^s, \mathbf{g}_{h,j}^s dx}{\int_{B_{h,j}^{n-1}} \mathbf{g}_{h,j}^{\text{init}}, \mathbf{g}_{h,j}^{\text{init}} dx} \leq \epsilon_{\text{tol}}, \quad 1 \leq j \leq N, \quad (7f)$$

we choose $\mathbf{v}_h^n = \mathbf{v}_h^s$ and $\lambda_{h,j}^n = \lambda_{h,j}^s$, $\mathbf{v}_j^{n-1/2} = \mathbf{v}_j^s$, $\boldsymbol{\omega}_j^{n-1/2} = \boldsymbol{\omega}_j^s$ for $1 \leq j \leq N$. Otherwise, we compute

$$\gamma_j^{s-1} = \frac{\int_{B_{h,j}^{n-1}} \mathbf{g}_{h,j}^s, \mathbf{g}_{h,j}^s dx}{\int_{B_{h,j}^{n-1}} \mathbf{g}_{h,j}^{s-1}, \mathbf{g}_{h,j}^{s-1} dx}, \quad 1 \leq j \leq N, \quad (7g)$$

and set

$$\mathbf{z}_{h,j}^s = \mathbf{g}_j^{s-1} - \gamma_j^{s-1} \mathbf{z}_j^{s-1}.$$

Finally, we set $s \rightsquigarrow s + 1$ and go back to the initialization step.

The last step of the splitting method is to update the particle. This is done by

$$\mathbf{C}_j^n = \mathbf{C}_j^{n-1} + \Delta t \mathbf{v}_j^n, \quad (8a)$$

$$\Theta_j^n = \Theta_j^{n-1} + \Delta t \boldsymbol{\omega}_j^n, \quad (8b)$$

$$\mathbf{v}_j^n = \mathbf{v}_j^{n-1/2} + \Delta t M_j^{-1} (\mathbf{F}_j^H + \mathbf{F}_j^r), \quad (8c)$$

$$\boldsymbol{\omega}_j^n = \boldsymbol{\omega}_j^{n-1/2} + \Delta t \mathbf{I}_j^{-1} (\mathbf{T}_j^H + (\overrightarrow{\mathbf{C}_j^n} \times \mathbf{F}_j^r)). \quad (8d)$$

4 Experimental Setup and Model Validation

The experimental setup consists of a fluid-filled container with an immersed SAW microchip at the ground. The SAW microchip is coated with a piezoelectric material such as lithium niobate (LiNbO_3) and features an Inter-Digital Transducer (IDT) placed at the center of the bottom of the container with its aperture pointing upwards (cf. Figure 2). Applying a high-frequency signal to the IDT, acoustic waves are generated that enter the fluid in the container and create a steady-state flow pattern at the fluid surface consisting of four counter-rotating vortices (cf. Figure 3). We note that the modeling, simulation, and optimization of piezoelectrically agitated acoustic streaming has been considered in [1, 2, 10, 13].

4.1 Generation of Pairwise Counter-Rotating Vortices

For the IDT, as piezoelectric material we have used 128° rotated **YX** lithium niobate (LiNbO_3). The operating frequency f of the IDT has been chosen according to $f_{\text{IDT}} = 1.42 \cdot 10^2$ MHz resulting in a maximum velocity $v_{\text{max}} = 2.0 \cdot 10^{-3}$ m/s on top of the water bulk with height $6.0 \cdot 10^{-4}$ m. The resulting SAW generated vorticity patterns consist of four pairwise counter-rotating vortices at the surface of the fluid, see Figure 3.

4.2 Production of L-shaped Enantiomers

For the production of the photoresist L-shaped enantiomers we have followed the protocol described by [12] with some modifications. The whole process of manufacturing is shown in Figure 4 and the numbers in parenthesis in the following text also refer to that figure.

First a sacrificial layer of omnicoat is spincoated on a silicon wafer (2). In a second spin coating process SU8-2 photoresist laden with 0.5 mg/ml Nile Red is spun onto the omnicoat layer at 3000 rounds per second achieving a film thickness of about $1.5 \mu\text{m}$ (3). After soft baking the photoresist it is exposed using a mask

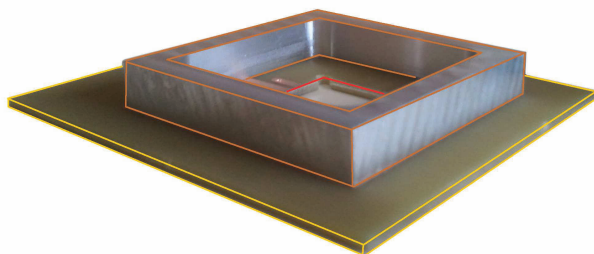


Figure 2. Side-view of the experimental setting (shown without water). The setup is mounted on a circuit board consisting of the fluid container and the IDT with substrate layer in the middle on the bottom of the water bulk.

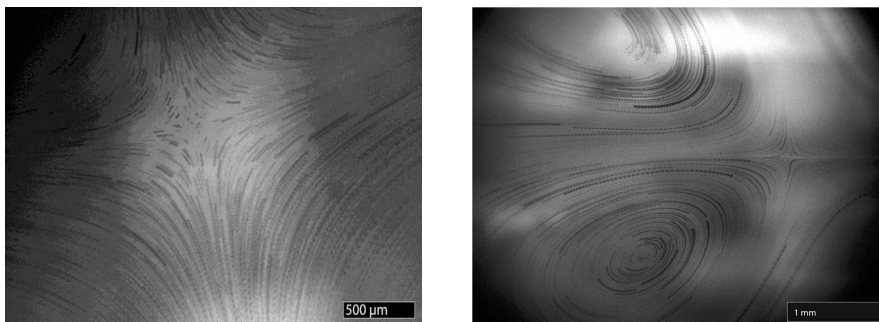


Figure 3. Left: Two-dimensional SAW generated surface streaming profile. The optical path is slightly tilted to gain a larger field of view. Hydrophobic coated beads of $1\ \mu\text{m}$ diameter were used as tracer particles to visualize the fluid flow on the surface. The image is a superposition of micrographs and shows parts of the four quadrant flows induced by the chip. Right: Micrograph showing two of the counter-rotating vortices. Diagonally opposing vortices always have the same direction of rotation.

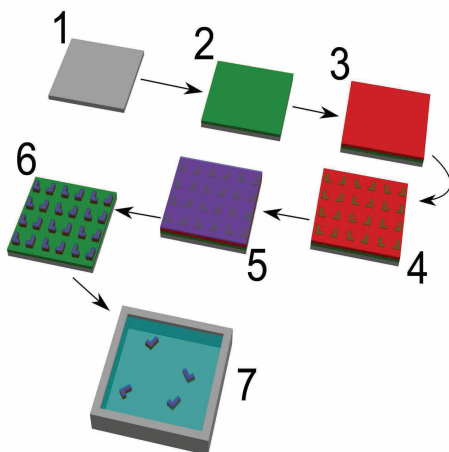


Figure 4. Schematic representation of fabrication of the photoresist particles. 1) Clean silicon wafer. 2) A sacrificial layer of omnicoat is applied. 3) SU8-2 is applied. 4) Photoresist is partially exposed. 5) Unexposed SU8-2 is developed. 6) Surface is treated with silane. 7) Lift-off. Afterwards particles are transferred onto the water surface and float stably in a well defined orientation.

aligner and then baked a second time (4). After the substrate has cooled to room temperature the unexposed photoresist is developed using MR-DEV300 leaving the desired particles attached to the sacrificial layer of omnicoat (5). In order to render the particles hydrophobic on one side a layer of Trichloro(octadecyl)silane (OTS) is applied by spin coating (6). To this end $10\ \mu\text{l}$ OTS are dissolved in 3 ml n-hexane and spun onto the particles at 1000 rpm for 10 seconds. The OTS solution has to be applied after the spin coater has reached its maximum rate of revolution since n-hexane evaporates very quickly thus leaving the OTS scattered on the surface inhomogeneously distributed if the spinning rate is too low. The layer of OTS renders the particles highly hydrophobic on the top side. After these steps the particles are still firmly attached to the substrate and can be stored in a dark ambient until use to prevent bleaching of the fluorescent dye. To remove the particles from the wafer, a lift-off procedure is performed using omnicoat developer. The wafer is immersed in the solution until the omnicoat layer has been sufficiently dissolved which takes approximately 30 seconds depending on the geometry of the sample. The wafer is then transferred to the experimental setup and the detached particles can be washed off using pure water. Due to the top side of the particles being considerably

Category/Name	Symbol	Unit	Value
Domain and Discretization			
Length	l_{Γ_s}	m	$8.4 \cdot 10^{-3}$
Grid Size	h	m	$2.1 \cdot 10^{-5}$
Time Step Size	Δt	s	$1.0 \cdot 10^{-2}$
Fluid (Water 25°C)			
Density	ρ	kg/m ³	$1.0 \cdot 10^3$
Dynamic Viscosity	η	Pa · s	$1.0 \cdot 10^{-3}$
Maximum Velocity	v_{\max}	m/s	$2.0 \cdot 10^{-3}$
Square Particle			
Length	l_S	m	$1.0 \cdot 10^{-4}$
Density	ρ_S	kg/m ³	$2.0 \cdot 10^3$
Center of Mass	C_S	m	$(8.6, 2.8)^T \cdot 10^{-4}$
Velocity	\mathbf{v}_S	m/s	$(-1.8, -3.5)^T \cdot 10^{-4}$
Angle of Rotation	Θ_S	rad	2.0
Angular Velocity	ω_S	rad/s	0.0
L-Shaped Particle			
Length	l_L	m	$2.3 \cdot 10^{-4}$
Density	ρ_L	kg/m ³	$2.0 \cdot 10^3$
Center of Mass	C_L	m	$(4.0, 2.3)^T \cdot 10^{-4}$
Velocity	\mathbf{v}_L	m/s	$(-1.3, -4.4)^T \cdot 10^{-4}$
Angle of Rotation	Θ_L	rad	5.3
Angular Velocity	ω_L	rad/s	0.0

Table 1. Domain, discretization, fluid and particle related constants and parameters for simulations validating the quadrupolar force density.

more hydrophobic than the bottom side the orientation of the particles is conserved during the lift off process in most cases and the particles float stably on the surface of the fluid.

4.3 Model Validation: Comparison with Experimental Measurements

In this section, we perform numerical simulations using the previously described fictitious domain Lagrange multiplier method. Here, we work with a quadrupolar force density as generating source of the fluid vorticity pattern consisting of pairwise counter-rotating vortices. Following [14], this source is given by

$$\mathbf{f} := -\eta \Delta \hat{\mathbf{v}}, \quad \hat{\mathbf{v}} = (\hat{v}_1, \hat{v}_2)^T, \quad \hat{v}_1 = \partial \Psi / \partial x_1, \quad \hat{v}_2 = -\partial \Psi / \partial x_2 \quad (9)$$

in terms of the stream function

$$\Psi(x_1, x_2) = v_{\max} \frac{l_{\Gamma_s} \sqrt{3}}{\pi} \frac{\sin(\pi x_1 / l_{\Gamma_s}) \sin(\pi x_2 / l_{\Gamma_s})}{(2 - \cos(\pi x_1 / l_{\Gamma_s})) (2 - \cos(\pi x_2 / l_{\Gamma_s}))},$$

where v_{\max} denotes the maximum velocity of the vector field.

A qualitative comparison shows that the SAW generated velocity field is close to the velocity field produced by the quadrupolar force field, see Figure 5. For model validation and verification of the numerical simulations, we have compared the trajectories of an L-shaped and a square shaped particle in the upper right quadrant of the surface of the fluid (counter-clockwise rotating vortex) obtained in an experiment and by numerical simulation. The corresponding numerical parameters are shown in Table 1. Figure 6 (left) displays the trajectories of the square shaped particle (red line) and the L-shaped particle (yellow line) in the experiment, whereas Figure 6 (right) shows the corresponding trajectories computed by the application of the FDLM using the data of the experimental set up. For a more quantitative comparison, we refer to Figure 7 which shows almost perfect agreement between experimental measurement and numerical simulation of the angle of rotation of the square shaped particle as a function of time.

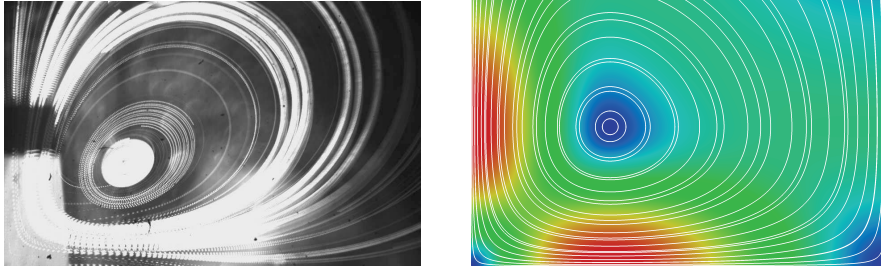


Figure 5. Left: Experimental SAW generated surface streaming profile with operating frequency $f_{\text{IDT}} = 1.42 \cdot 10^2$ MHz of the IDT. Right: Simulated vorticity pattern generated by a quadrupolar force field with $v_{\text{max}}(f_{\text{IDT}}) = 2.0 \cdot 10^{-3}$ m/s.

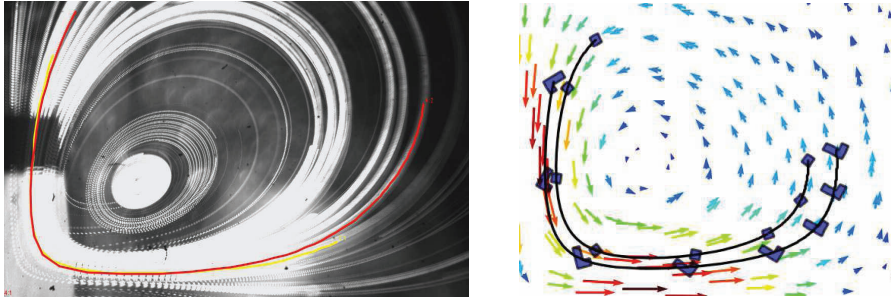


Figure 6. Left: Experimentally measured trajectories of a square shaped particle (red line) and an L-shaped particle (yellow line). Right: Computed trajectories based on the data of the experimental set up.

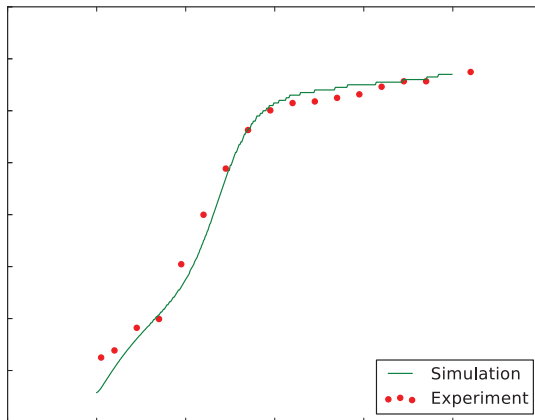


Figure 7. Angle of rotation of the particles as a function of time from Figure 6 (experiment: red dots, simulation: green line).

5 Numerical Simulation of Enantiomer Separation

Using the quadrupolar force density (9) we were able to reveal two qualitatively distinct cases of enantiomer separation in simulation. First, in Figure 8 we see the motion of a right-handed and a left-handed L-shaped enantiomer initially placed slightly left of the middle between two counter-rotating vortices in the lower quadrants of the surface of the fluid. As can be seen in Figure 8 (left), the right-handed enantiomer gets attracted by the counter-clockwise rotating vortex in the lower left quadrant. On the other hand, as shown in Figure 8 (right), the left-handed enantiomer follows a trajectory that leads to a path around the center of the clockwise rotating vortex in the upper left quadrant.

Likewise, Figure 9 shows that a right-handed (left-handed) enantiomer initially placed in the middle between the two counter-rotating vortices gets attracted by the counter-clockwise (clockwise) rotating vortex in the upper right (upper left) quadrant. In summary, right-handed (left-handed) enantiomers are attracted by counter-clockwise (clockwise) rotating vortices such that a perfect separation occurs provided the enan-

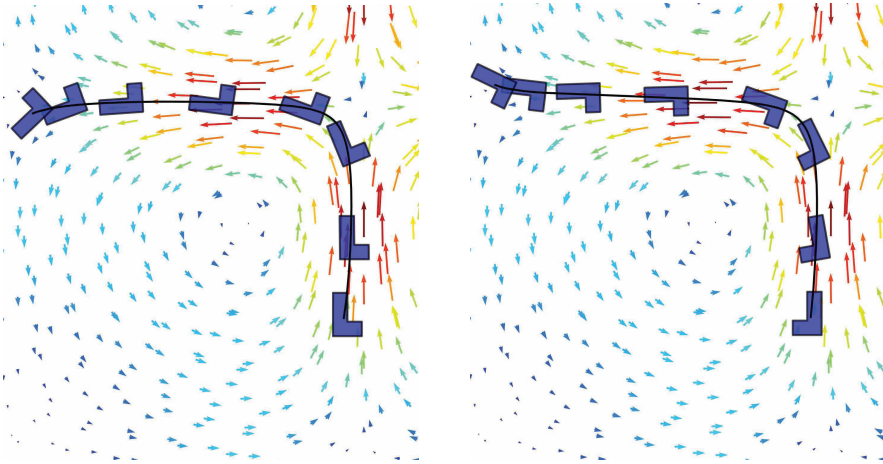


Figure 8. Enantiomer separation of a right-handed (left) and left-handed (right) L-shaped enantiomer at the outgoing velocity streamlines. The right-handed L-shaped particle follows the vortex rotating counter-clockwise in the lower left quadrant whereas the left-handed L-shaped particle follows the vortex rotating clockwise in the upper left quadrant.

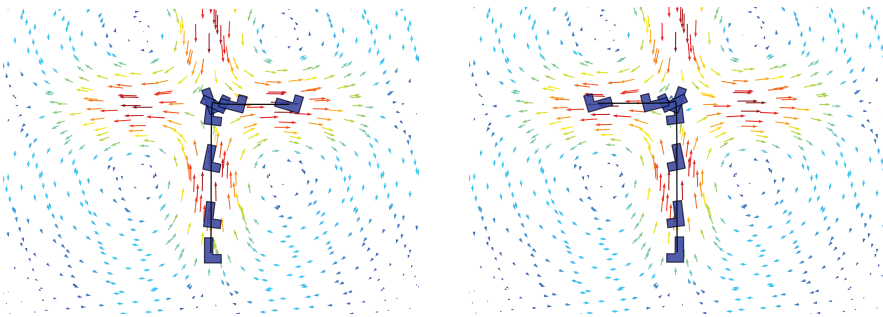


Figure 9. Enantiomer separation of a right-handed (left) and left-handed (right) L-shaped enantiomer at the central streamlines. The right-handed L-shaped particle follows the vortex rotating counter-clockwise in the upper right quadrant whereas the left-handed L-shaped particle follows the vortex rotating clockwise in the upper left quadrant.

tiomers are placed approximately in the middle between counter-rotating vortices. This general behavior is in accordance with the predictions for the highly idealized setting investigated in [14].

6 Conclusions

We have considered the numerical simulation of surface acoustic wave actuated separation of rigid enantiomers by the fictitious domain Lagrange multiplier method. The surface acoustic waves are generated by an Inter-Digital Transducer and create a flow pattern at the surface of the fluid which consists of four pairwise counter-rotating vortices. Enantiomers that are injected onto the surface approximately in the middle between two counter-rotating vortices are separated according to their handedness. As a mathematical model, we have used a coupled system in two space dimensions consisting of the incompressible Navier-Stokes equations and the rigid body equations of the immersed particles which are enforced by appropriately chosen Lagrange multipliers. A model validation has been performed by comparing experimental data and the results of numerical simulations. The separation mechanism is such that left-handed (right-handed) enantiomers are attracted by clockwise rotating (counter-clockwise rotating) vortices.

Funding: This work has been supported by the DFG Priority Program SPP 1506. R. H. W. Hoppe has been further supported by the DFG Priority Program SPP 1253, by the NSF grants DMS-0914788, DMS-1115658, and by the European Science Foundation within the Networking Programme OPTPDE.

References

- [1] H. Antil, A. Gantner, R. H. W. Hoppe, D. Köster, K. G. Siebert and A. Wixforth, Modeling and simulation of piezoelectrically agitated acoustic streaming on microfluidic biochips, in: *Proc. 17th Int. Conf. on Domain Decomposition Methods*, Lect. Notes Comput. Sci. Eng. 60, Springer, Berlin (2007), 305–312.
- [2] H. Antil, R. Glowinski, R. H. W. Hoppe, C. Linsenmann, T.-W. Pan and A. Wixforth, Modeling, simulation, and optimization of surface acoustic wave driven microfluidic biochips, *J. Comp. Math.* **28** (2010), 149–169.
- [3] K. Bester, Chiral analysis for environmental applications, *Anal. Bioanal. Chem.* **376** (2003), 302–304.
- [4] F. Brezzi and M. Fortin, *Mixed and Hybrid Finite Element Methods*, Springer, Berlin, 1991.
- [5] K. A. Busch and M. A. Busch (eds.), *Chiral Analysis*, Elsevier, Amsterdam, 2006.
- [6] A. J. Chorin, A numerical method for solving incompressible viscous flow problems, *J. Comput. Phys.* **2** (1967), 12–26.
- [7] A. N. Collins, G. Sheldrake and J. Crosby (eds.), *Chirality in Industry: The Commercial Manufacture and Applications of Optically Active Compounds*, Wiley, Chichester, 1995.
- [8] A. N. Collins, G. Sheldrake and J. Crosby (eds.), *Chirality in Industry II: The Commercial Manufacture and Applications of Optically Active Compounds*, Wiley, Chichester, 1997.
- [9] E. Francotte and W. Lindner (eds.), *Chirality in Drug Research*, Wiley-VCH, Weinheim, 2006.
- [10] A. Gantner, R. H. W. Hoppe, D. Köster, K. G. Siebert and A. Wixforth, Numerical simulation of piezoelectrically agitated surface acoustic waves on microfluidic biochips, *Comp. Visual. Sci.* **10** (2007), 145–161.
- [11] R. Glowinski, T.-W. Pan, T. I. Hesla, D. D. Joseph and J. Periaux, A fictitious domain approach to the direct numerical simulation of incompressible viscous flow past moving rigid bodies: Application to particulate flow, *J. Comput. Phys.* **169** (2001), 363–427.
- [12] C. J. Hernandez and T. G. Mason, Colloidal alphabet soup: Monodisperse dispersions of shape-designed lithoparticles, *J. Phys. Chem. C* **111** (2007), 4477–4480.
- [13] D. Köster, Numerical simulation of acoustic streaming on SAW-driven biochips, *SIAM J. Comp. Sci.* **29** (2007), 2352–2380.
- [14] M. Kostur, M. Schindler, P. Talkner and P. Hänggi, Chiral separation in microflows, *Phys. Rev. Lett.* **96** (2006), 014502-1–014502-4.
- [15] N. Kurihara and J. Miyamoto (eds.), *Chirality in Agrochemicals*, Wiley, Chichester, 1998.
- [16] P. C. H. Li, *Microfluidic Lab-on-a-Chip for Chemical and Biological Analysis and Discovery*, CRC Press, Boca Raton, 2006.
- [17] G. I. Marchuk, Splitting and alternating direction methods, in: *Handbook of Numerical Analysis, Vol. 1*, North-Holland, Amsterdam (1990), 197–462.
- [18] Marcos, H. Fu, T. R. Powers and R. Stocker, Separation of microscale chiral objects by shear flow, *Phys. Rev. Lett.* **102** (2009), 158103-1–158103-4.
- [19] T.-W. Pan, R. Glowinski and D. D. Joseph, Simulating the dynamics of fluid-ellipsoid interactions, *Comput. Struct.* **83** (2005), 463–478.
- [20] M. Quack, J. Strohner and M. Willeke, High-resolution spectroscopic studies and theory of parity violation in chiral molecules, *Ann. Rev. Phys. Chem.* **59** (2008), 741–769.
- [21] G. K. E. V. Scriba, Cyclodextrins in capillary electrophoresis enantioseparations: Recent developments and applications, *J. Sep. Sci.* **31** (2008), 1991–2011.
- [22] L. Tartar, *Introduction to Sobolev Spaces and Interpolation Theory*, Springer, Berlin, 2007.
- [23] R. Temam, Une methode d'approximation de la solution des equations de Navier-Stokes, *Bull. Soc. Math. France* **98** (1968), 115–152.
- [24] T. Wang, T.-W. Pan, Z. W. Xing and R. Glowinski, Numerical simulation of rheology of red blood cell rouleaux in microchannels, *Phys. Rev. E* **79** (2009), 041916-1–041916-11.
- [25] C. J. Welch, Microscale chiral HPLC in support of pharmaceutical process research, *Chirality* **21** (2009), 114–118.
- [26] T. J. Wenzel, *Discrimination of Chiral Compounds using NMR Spectroscopy*, Wiley, Chichester, 2007.